

## Energetic-particle-driven instabilities and induced fast-ion transport in a reversed field pincha)

L. Lin, J. K. Anderson, D. L. Brower, W. Capecchi, W. X. Ding, S. Eilerman, C. B. Forest, J. J. Kollner, D. Liu, M. D. Nornberg, J. Reusch, and J. S. Sarff

Citation: *Physics of Plasmas* (1994-present) **21**, 056104 (2014); doi: 10.1063/1.4872029

View online: <http://dx.doi.org/10.1063/1.4872029>

View Table of Contents: <http://scitation.aip.org/content/aip/journal/pop/21/5?ver=pdfcov>

Published by the [AIP Publishing](#)

---

### Articles you may be interested in

[Fast ion confinement and stability in a neutral beam injected reversed field pincha\)](#)

*Phys. Plasmas* **20**, 056102 (2013); 10.1063/1.4801749

[Measurement of energetic-particle-driven core magnetic fluctuations and induced fast-ion transport](#)

*Phys. Plasmas* **20**, 030701 (2013); 10.1063/1.4798397

[Modulated active charge exchange fast ion diagnostic for the C-2 field-reversed configuration experimenta\)](#)

*Rev. Sci. Instrum.* **83**, 10D720 (2012); 10.1063/1.4732853

[Density fluctuation measurements by far-forward collective scattering in the MST reversed-field pincha\)](#)

*Rev. Sci. Instrum.* **83**, 10E302 (2012); 10.1063/1.4728098

[Collective fast ion instability-induced losses in National Spherical Tokamak Experimenta\)](#)

*Phys. Plasmas* **13**, 056109 (2006); 10.1063/1.2178788

---



### Vacuum Solutions from a Single Source

- Turbopumps
- Backing pumps
- Leak detectors
- Measurement and analysis equipment
- Chambers and components

**PFEIFFER**  **VACUUM**

# Energetic-particle-driven instabilities and induced fast-ion transport in a reversed field pinch<sup>a)</sup>

L. Lin,<sup>1,b)</sup> J. K. Anderson,<sup>2</sup> D. L. Brower,<sup>1</sup> W. Capecchi,<sup>2</sup> W. X. Ding,<sup>1</sup> S. Eilerman,<sup>2</sup> C. B. Forest,<sup>2</sup> J. J. Koliner,<sup>2</sup> D. Liu,<sup>3</sup> M. D. Nornberg,<sup>2</sup> J. Reusch,<sup>2</sup> and J. S. Sarff<sup>2</sup>

<sup>1</sup>Department of Physics and Astronomy, University of California Los Angeles, Los Angeles, California 90095, USA

<sup>2</sup>Department of Physics, University of Wisconsin–Madison, Madison, Wisconsin 53706, USA

<sup>3</sup>Department of Physics and Astronomy, University of California Irvine, Irvine, California 92697, USA

(Received 22 November 2013; accepted 23 January 2014; published online 25 April 2014)

Multiple bursty energetic-particle (EP) driven modes with fishbone-like structure are observed during 1 MW tangential neutral-beam injection in a reversed field pinch (RFP) device. The distinguishing features of the RFP, including large magnetic shear (tending to add stability) and weak toroidal magnetic field (leading to stronger drive), provide a complementary environment to tokamak and stellarator configurations for exploring basic understanding of EP instabilities. Detailed measurements of the EP mode characteristics and temporal-spatial dynamics reveal their influence on fast ion transport. Density fluctuations exhibit a dynamically evolving, inboard-outboard asymmetric spatial structure that peaks in the core where fast ions reside. The measured mode frequencies are close to the computed shear Alfvén frequency, a feature consistent with continuum modes destabilized by strong drive. The frequency pattern of the dominant mode depends on the fast-ion species. Multiple frequencies occur with deuterium fast ions compared to single frequency for hydrogen fast ions. Furthermore, as the safety factor ( $q$ ) decreases, the toroidal mode number of the dominant EP mode transits from  $n = 5$  to  $n = 6$  while retaining the same poloidal mode number  $m = 1$ . The transition occurs when the  $m = 1$ ,  $n = 5$  wave-particle resonance condition cannot be satisfied as the fast-ion safety factor ( $q_{fi}$ ) decreases. The fast-ion temporal dynamics, measured by a neutral particle analyzer, resemble a classical predator-prey relaxation oscillation. It contains a slow-growth phase arising from the beam fueling followed by a rapid drop when the EP modes peak, indicating that the fluctuation-induced transport maintains a stiff fast-ion density profile. The inferred transport rate is strongly enhanced with the onset of multiple EP modes. © 2014 AIP Publishing LLC. [<http://dx.doi.org/10.1063/1.4872029>]

## I. INTRODUCTION

Energetic particle (EP) physics is a critical component in magnetic confinement fusion research.<sup>1,2</sup> In toroidal plasma devices, large populations of super-thermal EPs are born from radio-frequency heating, neutral beam injection (NBI), and fusion reactions.<sup>3,4</sup> Various forms of instabilities can be driven unstable by spatial and velocity gradients of the EP distribution function. Because of strong interactions with fast ions, the fluctuating electric and magnetic fields arising from these instabilities can cause significant and concentrated EP redistribution and losses that not only degrade confinement but can also damage the vacuum vessel and plasma-facing components.<sup>5</sup>

Compared to other toroidal configurations (tokamaks, spherical tokamaks, and stellarators),<sup>6</sup> knowledge of EP-driven instabilities and their impact on fast-ion confinement is only recently emerging for the reversed field pinch (RFP) magnetic configuration. Unique features of the RFP configuration render it a new and complementary environment to test and challenge our basic understanding of these instabilities. The strongly twisted magnetic field lines result in large

magnetic shear that tends to stabilize instabilities, while the weak toroidal magnetic field leads to larger fast ion  $\beta_f$  (ratio of fast-ion pressure to magnetic pressure) that induces stronger drive.<sup>7</sup> Ubiquitous tearing modes present in the RFP make it a good candidate to explore the interaction between fast ions and global MHD instabilities. Furthermore, under special conditions, a spontaneously generated 3D helical equilibrium<sup>8</sup> makes the RFP an interesting configuration to study non-axisymmetric equilibrium effects on EP confinement.<sup>9</sup> In addition to the above mentioned opportunities to connect with and contribute to other toroidal configurations, understanding of EP physics in the RFP is a vital component in evaluating its fusion potential.

The first observation of Alfvén eigenmodes (AEs) in a RFP was from the Extrap-T2R device that did not have an EP population. The measured instabilities exhibited features consistent with the toroidicity-induced Alfvén eigenmodes (TAEs) and their coupling with the electron drift turbulence was proposed as the destabilization mechanism.<sup>10</sup> Alfvénic eigenmodes in a RFP have also been detected in the purely ohmic-heated RFX-mod device. In this case, the mode was interpreted as the global Alfvén eigenmode (GAE) and the driving mechanism was speculated to be the fast ions generated during the spontaneous magnetic reconnection<sup>11</sup> where large magnetic energy is released.<sup>12</sup>

<sup>a)</sup>Paper N12 1, Bull. Am. Phys. Soc. **58**, 188 (2013).

<sup>b)</sup>Invited speaker.

The first observation of the EP-instabilities in a RFP excited with a clear fast-ion source is from the Madison Symmetric Torus (MST) device where fast ions are generated by a 1 MW neutral beam injector.<sup>13</sup> Internal structure of the excited instabilities is measured with a combined interferometry-polarimetry diagnostic, including first direct observation of internal magnetic fluctuations associated with EP instabilities.<sup>14</sup> The density fluctuations exhibit dynamically evolving, inboard-outboard asymmetric spatial pattern. Detailed analysis also reveals strong nonlinear three-wave coupling among multiple modes. Fast-ion measurements with a neutral particle analyzer suggest that these EP instabilities can greatly reduce fast-ion density below the value expected from classical predictions.

The goal of this paper is to provide an overview of EP-instabilities and associated fast-ion transport in the MST-RFP plasmas. The paper is organized as follows. Section II describes the MST device, neutral beam injector, and major diagnostics. Section III describes classical modeling of the fast-ion distribution and analytical calculation of Alfvén continua. Section IV characterizes EP-fluctuation measurements and their dependence on plasma/beam species, and safety factor profile. A subsection is also included in Sec. IV to describe the fluctuation-induced fast-ion transport. Section V contains the summary with some discussions.

## II. EXPERIMENTAL SETUP

The MST is a toroidal magnetic confinement device with major radius  $R_0 = 1.5$  m and minor radius  $a = 0.52$  m.<sup>15</sup> It typically operates with toroidal plasma current ( $I_\phi$ ) of 200–600 kA, central line-averaged electron density ( $\bar{n}_e$ ) of  $0.4$ – $1.5 \times 10^{19} \text{ m}^{-3}$ , and core electron temperature of 200–2000 eV. The major working gas is deuterium (D), which can be switched to hydrogen (H) to expand the experimental range of Alfvén velocity,  $v_A = B/\sqrt{\mu_0 \rho}$ , where  $B$  is the magnetic field strength,  $\mu_0$  is the vacuum permeability, and  $\rho$  is the plasma mass density.

The safety factor ( $q$ ) is a critical parameter in EP physics,<sup>3,4</sup>  $q = rB_\phi/RB_\theta$ , where  $r$  is the minor radius,  $R$  is the major radius,  $B_\theta$  is the poloidal magnetic field, and  $B_\phi$  is the toroidal magnetic field. The  $q$  value in a RFP is quite different from that of a tokamak, remaining much less than 1 throughout the plasma cross section. The  $q$  profile can be tuned by varying the reversal parameter ( $F$ ), which is defined as the ratio of the edge  $B_\phi$  to the volume-averaged  $B_\phi$ ,  $F = B_\phi(a)/\langle B_\phi \rangle$ . Figure 1(a) shows the  $q$  profiles for various  $F$ -value plasmas where  $I_\phi = 300$  kA and  $\bar{n}_e \sim 0.7 \times 10^{19} \text{ m}^{-3}$ . The local density profiles ( $n_e$ ) are shown in Fig. 1(b). The uncertainty of reconstructed local  $n_e$  is below 10%. As  $F$  is reduced from 0 to  $-0.4$ , the central  $q$  value ( $q_0$ ) drops from 0.21 to 0.17 and the edge  $q$  value ( $q_a$ ) decreases from 0 to  $-0.07$ , which has a significant impact on resonant tearing instabilities. Reduction of  $q_0$  below 0.2 serves to remove the internal resonant surface of the  $m = 1$ ,  $n = 5$  global tearing mode at  $q = m/n$ , where  $m$  is the poloidal mode number and  $n$  is the toroidal mode number. The impact of the  $q$  profiles on the EP instabilities will be described later in Sec. IV C.

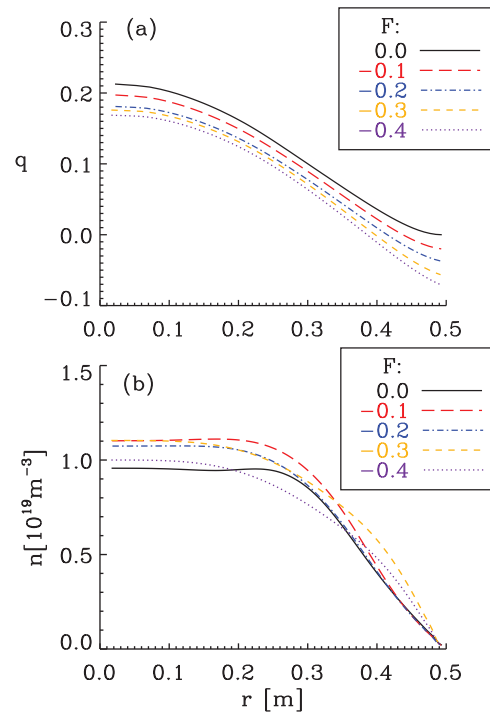


FIG. 1. Profiles of (a) safety factor and (b) electron density for various  $F$  values in D-plasmas where  $I_\phi \sim 300$  kA,  $\bar{n}_e \sim 0.7 \times 10^{19} \text{ m}^{-3}$ , and 40 A H-beam at 24 kV is injected.

Positive fast ions are generated by a 1 MW neutral beam that tangentially (with the tangency  $R = 1.41$  m) injects fast neutrals with energy ( $E$ ) up to 25 kV.<sup>16,17</sup> The beam fuel can be hydrogen (H) or deuterium (D), a practical knob to explore dependence of EP instabilities on  $v_B/v_A$ , where  $v_B = \sqrt{2E/m_B}$  is the beam ion velocity. The energy ( $E : E/2 : E/3 : E/18$ ) fractions of injected fast ions are 86% : 10% : 2% : 2%. Those fractions are not expected to strongly depend on beam species or acceleration voltage. This is particularly true for the full-energy components, as it is most relevant to the results presented in this paper. Co- or counter-current ( $I_\phi$ ) injection is achieved by reversing the plasma current direction. In this paper, only co-current NBI is used as the confinement of fast ions from counter-current injection is relatively poor and prompt losses are large.<sup>17</sup>

All measurements reported herein are for plasmas with  $I_\phi \sim 300$  kA and  $\bar{n}_e \sim 0.7 \times 10^{19} \text{ m}^{-3}$  while varying other plasma parameters, including plasma species (H or D), fast-ion species, and  $q$  profile. The core electron temperature is  $\sim 260$  eV. The tearing mode amplitude is small and the level of radial magnetic fluctuations ( $\bar{b}_r/B$ ) remains  $< 2\%$  across the whole minor radius. The plasma equilibrium remains approximately axisymmetric with nested circular flux surfaces.

The fluctuation diagnostics employed include a toroidal array of 32 Mirnov coils and a poloidal array of 8 coils with temporal resolution  $1 \mu\text{s}$ . These coils are located on the inner surface of the vacuum vessel ( $r \sim a$ ). Toroidal mode number ( $n$ ) and poloidal mode number ( $m$ ) are resolved by spatially decomposing the measured magnetic fluctuations.

The primary internal equilibrium and fluctuation diagnostic is a multi-chord Faraday-effect polarimetry-interferometry system,<sup>18</sup> which measures line-integrated electron density

$$\Phi = 2.82 \times 10^{-15} \lambda_0 \int n_e dz \quad (1)$$

and Faraday rotation

$$\Psi_p = 2.62 \times 10^{-13} \lambda_0^2 \int n_e B_{\parallel} dz, \quad (2)$$

where  $\lambda_0 = 432 \mu\text{m}$  is the wavelength of the probe beam,  $n_e$  is the electron density,  $B_{\parallel}$  is the magnetic field parallel to the beam propagation direction, and  $z$  is the distance along the probe beam in the plasma, all in MKS units. This laser-based system consists of 11 vertically viewing chords (with a chord separation  $\sim 0.08$  m along the major radius) covering most of the plasma cross section. High-speed<sup>19</sup> and high accuracy<sup>20</sup> capabilities permit reliable measurements of equilibrium and fluctuating quantities with a temporal resolution up to  $1 \mu\text{s}$ . The equilibrium interferometry-polarimetry measurements provide critical constraints in the reconstruction of local density and magnetic profiles, which are crucial to identification of the EP modes and exploration of the damping mechanism. The safety-factor and density profiles in Fig. 1 are from equilibrium reconstruction using the MSTFit<sup>21</sup> code constrained by interferometry-polarimetry and global magnetic field measurements. The line-integrated fluctuation measurements provide details on the internal structure of density and magnetic fluctuations associated with the EP instabilities. This serves to make the characterization of the EP-mode amplitude more reliable.<sup>22–24</sup> Toroidal and poloidal mode numbers of measured interferometry and polarimetry fluctuations can be resolved from cross-correlation with the spatially decomposed edge magnetic fluctuations.

Fast-ion dynamics are identified using a high-energy advanced neutral particle analyzer (ANPA), which measures the fast neutrals arising from the charge exchange between fast ions and the background neutrals.<sup>25</sup> The ANPA diagnostic can simultaneously measure fast hydrogen and deuterium ions up to  $\sim 35$  keV with energy resolution 2–4 keV and temporal resolution  $10 \mu\text{s}$ . The compact size of the ANPA allows physical repositioning between radial and tangential views which are sensitive to different portions of fast ion distribution in the phase space. In this paper only the tangential view, which is primarily sensitive to the circulating fast ions near the plasma core, is used.<sup>26</sup> In addition to the ANPA diagnostic, the amplitude and temporal dynamics of the global tearing modes can also be used as an indirect diagnostic of fast ions. NBI has been observed to reduce the core-most resonant tearing-mode amplitude by up to 60%.<sup>14</sup> This reduction exhibits a linear correlation with the ANPA signal and provides an indirect measure of fast ions when the ANPA measurement is not available or its interpretation is complicated by the background neutrals and the slowing-down process.<sup>26</sup>

### III. NUMERICAL CALCULATIONS

#### A. Fast-ion distribution modeling

The NUBEAM module of the TRANSP code<sup>27,28</sup> has been used to model the fast-ion distribution function. The

modeling considers classical behavior of fast ions, and charge exchange loss with background neutrals is found to be the main classical loss mechanism. Figure 2(a) shows the modeled time-dependent fast-ion density profile. The H-beam (40 A and 24 kV) is tangentially injected in the co-current direction from 20 to 40 ms into D-plasmas. Currently, only  $F = 0$  plasmas can be reliably modeled, as TRANSP requires monotonic toroidal flux, which is violated for conventional RFP equilibria with  $F < 0$ . The fast ion density profile is centrally peaked and  $>75\%$  of fast ions reside inside  $r/a = 0.5$ . Furthermore, fast ions are dominated by circulating particles with high velocity pitch,  $v_{\parallel}/v \sim 0.9$ , primarily due to the tangential injection geometry.

Time evolution of the modeled central fast ion density ( $n_{fi}$ ), shown in Fig. 2(b), can be simply described using

$$\frac{\partial n_{fi}}{\partial t} = S - \frac{n_{fi}}{\tau}, \quad (3)$$

where  $S$  is the constant source term from beam fueling and  $\tau$  describes classical losses. Solving Eq. (3) with  $S = 4 \times 10^{17} \text{m}^{-3} \text{ms}^{-1}$  and  $\tau = 6.2$  ms gives the  $n_{fi}$  value that best matches the TRANSP output. Furthermore,  $\tau = 6.2$  ms is close to the fast-ion confinement time measured from low-beam concentration (no excitation of instabilities) experiments using the beam blip method.<sup>29</sup>

As in Figure 2(b), the classically predicted core fast ion density saturates at  $\sim 2.5 \times 10^{18} \text{m}^{-3}$  after  $\sim 18$  ms injection (40 A), which is  $\sim 25\%$  of the core electron density ( $n_{e0} \sim 1 \times 10^{19} \text{m}^{-3}$ ). In reality, however, the core fast ion density is expected to be below the classical prediction, as instabilities occur  $\sim 2.5$  ms after beam injection (Sec. IV). With the onset of instabilities, a quasi-steady state with the core fast-ion density  $\sim 0.8 \times 10^{18} \text{m}^{-3}$  is generated where continuous beam fueling is balanced by fluctuation-induced transport. This picture is partially confirmed by reducing the beam current from 40 A to 24 A. With the reduced injection rate,  $\sim 4.7$  ms is needed to classically fuel the core density to

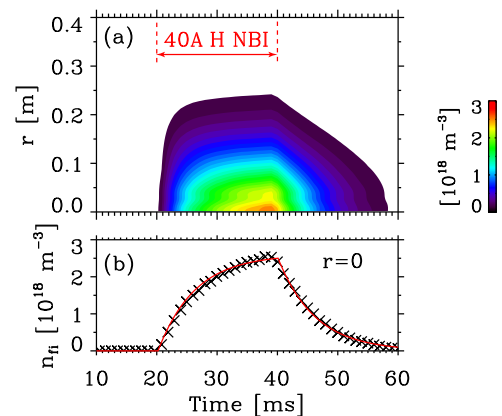


FIG. 2. TRANSP modeling of injected 40 A H-beam at 24 kV (from 20 to 40 ms) into D-plasma ( $I_{\phi} \sim 300$  kA,  $\bar{n}_e \sim 0.7 \times 10^{19} \text{m}^{-3}$ , and  $q_a = 0$ ): (a) fast-ion density profile (integrated over velocity phase space), (b) core fast ion density temporal evolution, where the cross (x) symbols are from the TRANSP modeling and solid red curve is from solving Eq. (3) for  $S = 4 \times 10^{17} \text{m}^{-3} \text{ms}^{-1}$  and  $\tau = 6.2$  ms.

$\sim 0.8 \times 10^{18} \text{ m}^{-3}$ , which is roughly consistent with the  $\sim 4.5 \text{ ms}$  onset time of EP instabilities in this case. Consequently, the core fast-ion density is expected to be  $\sim 0.8 \times 10^{18} \text{ m}^{-3}$ , about  $\sim 8\%$  of the core electron density. The corresponding core fast-ion  $\beta_f$  is  $\sim 3\%$ , exceeding the core thermal plasma  $\beta_0 \sim 2\%$  (ratio of bulk plasma pressure to magnetic pressure).

Fast ion orbits in RFPs can be quite different from that of thermal particles following the magnetic field lines. A fast-ion safety factor ( $q_{fi}$ ) is useful to describe this feature<sup>30,31</sup>

$$q_{fi} = \frac{rv_\phi}{Rv_\theta}, \quad (4)$$

where  $v_\phi$  and  $v_\theta$  are toroidal and poloidal guiding center velocities of fast ions. In RFPs,  $q_{fi}$  can be quite different from the magnetic field line safety factor  $q$ , while  $q_{fi} \approx q$  in tokamaks. Figure 3 shows comparison of  $q$  and  $q_{fi}^{H,D}$  for a  $I_\phi = 300 \text{ kA}$  and  $F = 0$  plasma, where H- and D-ions with energy 24 kV and velocity pitch 0.9 are used to calculate  $q_{fi}^{H,D}$ . These  $q$  profiles are obtained by equilibrium reconstruction constrained by internal magnetic-field measurements from the multi-chord polarimetry diagnostic. Estimated error is below 10%. The fast-ion safety factor also exhibits a dependence on the fast-ion species, as  $q_{fi}^D$  remains everywhere above  $q_{fi}^H$  and both are significantly larger than  $q$ .

The fast-ion safety factor is related to the resonant interactions between MHD modes and fast ions. Efficient power transfer between the fast-ion kinetic energy and the wave energy residing in the instabilities requires satisfying the resonance condition<sup>32</sup>

$$f \approx nf_\phi - (m+l)f_\theta, \quad (5)$$

where  $f$  is the mode frequency, integer  $l$  comes from the poloidal decomposition of fast-ion fluctuating velocity, and  $f_\theta$  and  $f_\phi$  are the fast-ion poloidal and toroidal transit frequencies, respectively. The fast-ion  $q_{fi}$  defined in Eq. (4) can be also written as

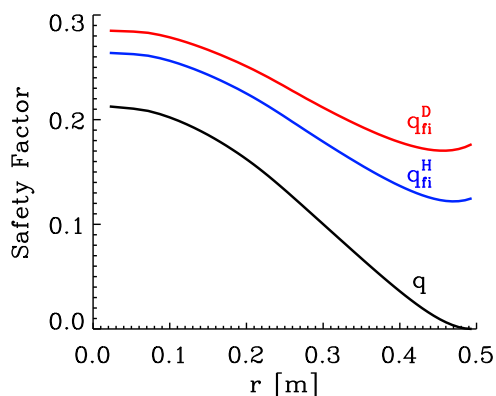


FIG. 3. Safety factor profiles for magnetic field lines ( $q$ , black), H fast-ion ( $q_{fi}^H$ , blue), and D fast-ion ( $q_{fi}^D$ , red) at energy  $E = 24 \text{ kV}$  and velocity pitch  $v_{||}/v = 0.9$ . The plasma equilibrium is for discharges with  $I_\phi \sim 300 \text{ kA}$ ,  $\bar{n}_e \sim 0.7 \times 10^{19} \text{ m}^{-3}$ , and  $q_a = 0$ .

$$q_{fi} = \frac{f_\phi}{f_\theta}. \quad (6)$$

The resonance condition in Eq. (5) can be rewritten as

$$q_{fi} \approx \frac{m+l}{n-f/f_\phi}. \quad (7)$$

This equation will be used to address the resonance condition for the observed EP-instabilities.

## B. Alfvén continuum calculations

Modeling predicts a core-localized fast-ion spatial distribution for MST parameters, as shown in Fig. 2(a), which naturally leads to a strong radial gradient that may excite AEs. One well-known AE candidate is the TAE, which occurs in a gap in the continuous Alfvén wave spectrum. The gap is formed as a consequence of toroidal coupling of shear Alfvén waves with toroidal mode number  $n$  and poloidal mode numbers  $m$  and  $m+1$ . The expected TAE frequencies are readily calculated from the dispersion relation derived for the RFP configuration<sup>10</sup>

$$\omega^2(r) = k_{||,m}^2(r)v_A^2(r)\gamma(r), \quad (8)$$

where  $v_A$  is the Alfvén velocity,

$$k_{||}(r) = \left[ \frac{m-nq(r)}{r} \right] \frac{B_\theta(r)}{B(r)} \quad (9)$$

is the wavevector component parallel to the magnetic field,

$$\gamma = \frac{1 + \sigma \pm \sqrt{(1-\sigma)^2 + \varepsilon_0^2 \sigma}}{2 - \varepsilon_0^2/2} \quad (10)$$

and  $\sigma = k_{||,m+1}^2/k_{||,m}^2$ . The TAE gap opening is essentially described by

$$\varepsilon_0 = 2\frac{r}{R_0} + 2\Delta' \left( \frac{q^2}{q^2 + r^2/R_0^2} \right), \quad (11)$$

where  $\Delta'$  is the radial derivative of the Shafranov shift. For typical MST plasmas,  $\varepsilon_0 \approx 2r/R_0$ . As  $\varepsilon_0 \rightarrow 0$ , two branches of Eq. (8) reduce to the  $m$  and  $m+1$  shear Alfvén dispersion relations in the cylindrical approximation, i.e.,  $\omega^2 = k_{||,m+1}^2 v_A^2$  and  $\omega^2 = k_{||,m}^2 v_A^2$ .

Figure 4 shows the calculated Alfvén continua for  $n = 4, 5, 6$  using Eq. (8) for plasma equilibrium at two different reversal parameters, which correspond to two separate  $q$  profiles. The coupling is between  $m = 0$  and 1. As seen in Fig. 4(a) at  $F = 0$  and  $q_a = 0$ , the TAE gaps exist near the locations where the safety factor  $q_{gap} = 0.5/n$ . As  $n$  increases and  $q_{gap}$  decreases, the gap location moves slightly outward to match the decreasing  $q$  profile. The gap frequency also slightly decreases as  $n$  increases but remains above 200 kHz. Similar features exist for the  $F = -0.4$  and  $q_a = -0.07$  case, where larger gap frequencies are displaced to further inboard locations arising from the globally reduced

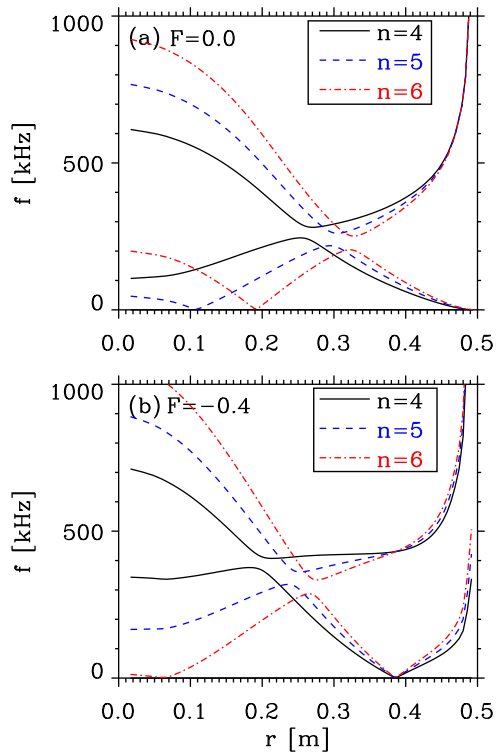


FIG. 4. The  $n = 4, 5, 6$  Alfvén continua (coupling of  $m = 0, 1$ ) for D-plasma equilibria with (a)  $F = 0$  and (b)  $F = -0.4$ , where  $I_\phi \sim 300$  kA and  $\bar{n}_e \sim 0.7 \times 10^{19} \text{ m}^{-3}$ .

$q$ -profile across the whole minor radius [Fig. 1(a)]. One pronounced difference for the  $F = -0.4$  case is that the  $n = 5, 6$  TAE gaps are not open across the entire minor radius. Gap frequencies cross the Alfvén continuum outside the reversal surface ( $q = 0$ ) [see Fig. 1(a)], leading to increased damping near the plasma edge.

## IV. EXPERIMENTAL RESULTS

### A. Fluctuation measurements

Energetic particle instabilities are routinely observed by multiple diagnostics in NBI-heated MST RFP plasmas.<sup>13,14</sup> Figure 5 shows an example from a deuterium plasma discharge with plasmas current  $I_\phi \sim 300$  kA, central line-averaged density  $\bar{n}_e \sim 0.7 \times 10^{19} \text{ m}^{-3}$ ,  $F = 0$ , and edge safety factor  $q_a = 0$ . This type of plasma is well-diagnosed and used to explore the characteristics of excited EP-modes. As shown in Fig. 5, high-frequency ( $>50$  kHz)  $n = 5$  poloidal magnetic fluctuations with a broad frequency peak centered at  $\sim 90$  kHz are detected by external magnetic coils  $\sim 2.5$  ms after the onset of hydrogen neutral beam injection. The mode has a bursty nature and decays away within 1 ms of NBI turnoff. The lower-frequency ( $<30$  kHz) mode, which is observed with no NBI present, corresponds to an  $n = 5$  global tearing mode destabilized by the current density gradient. The measured frequency in the lab frame ( $f_L$ ) contains contributions from the mode frequency in the plasma frame ( $f_P$ ) and the Doppler-shifted frequency ( $f_D$ ) due to the plasma rotation ( $v$ )

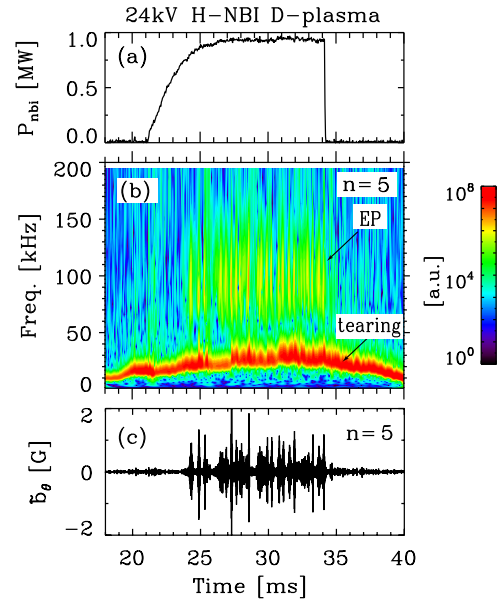


FIG. 5. Time traces of (a) 24 kV H-beam power, (b) spectrogram (in the lab frame) of the  $n = 5$  poloidal magnetic fluctuation measured at the plasma wall using external coils, and (c) high-frequency  $n = 5$  poloidal magnetic fluctuation after applying bandpass frequency filter from 60 to 120 kHz.

$$f_L = f_P + f_D = f_P + \frac{\mathbf{k} \cdot \mathbf{v}}{2\pi}, \quad (12)$$

where  $v$  is inferred from the tearing mode rotation speed, which is consistent with spectroscopic measurements.<sup>33</sup> After correcting for  $f_D$ , the  $n = 5$  EP mode frequency peak is reduced to  $\sim 65$  kHz in the plasma frame, which is significantly below the predicted TAE frequency 200–300 kHz (Fig. 4). Previous frequency-scaling studies revealed that the  $n = 5$  mode frequency shows some dependence on the beam ion velocity but weak dependence on the Alfvén velocity,<sup>13</sup> suggesting a non-eigenmode identity. To better examine the temporal dynamics, Fig. 5(c) shows the time trace of the  $n = 5$  magnetic fluctuation after bandpass filtering from 60 to 120 kHz. The mode exhibits a quasi-periodic bursty character with burst period roughly  $\sim 0.4$  ms and burst duration  $\sim 0.06$  ms (amplitude above half maximum). The  $\sim 0.06$  ms duration corresponds to  $\sim 160$  Alfvén times ( $\tau_A = a/v_A$ ), which is comparable to the typical interaction time between strongly excited energetic particle continuum modes (EPMs) and resonant fast ions.<sup>34</sup> The temporal peak of the  $n = 5$  mode amplitude has practical application in data processing, as it provides a convenient and accurate time marker to combine many similar events for the purpose of employing averaging techniques to reduce noise and to enable fluctuation-correlation analysis to extract the mode number.<sup>35,36</sup> All fluctuation analyses presented herein, except when explicitly specified, are ensembled over many similar events in the time window from  $-0.2$  to  $0.2$  ms using the burst amplitude peak of the dominant mode as the time reference ( $t = 0$ ).

Detailed examination of the measured magnetic fluctuations reveals that multiple EP-driven modes are present. Figure 6 shows the frequency vs. toroidal mode number ( $|n|$ )

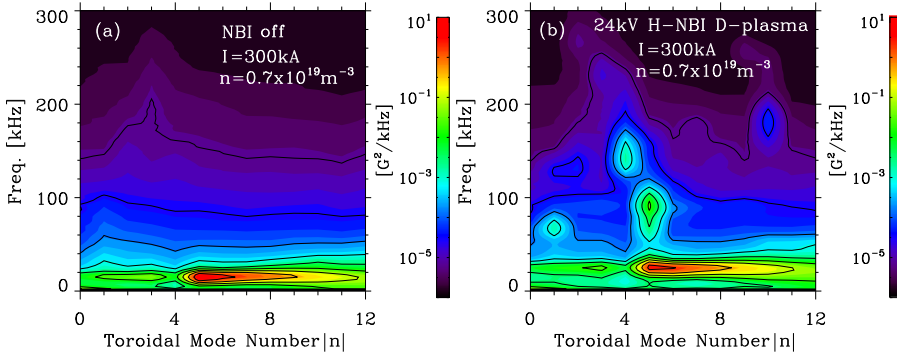


FIG. 6. Frequency (in the lab frame) variation with toroidal mode number ( $|n|$ ) of poloidal magnetic fluctuations for plasmas (a) without NBI and (b) with 24kV and 40 A H-NBI, where  $I_\phi \sim 300$  kA,  $\bar{n}_e \sim 0.7 \times 10^{19} \text{ m}^{-3}$ , and edge  $q_a = 0$  for both cases.

spectra for plasmas with and without NBI. In the spatial decomposition of magnetic fluctuations from the toroidal array, the sign of  $n$  can also be determined after further examination and is specified for the dominant modes. Positive  $n$  corresponds to the mode toroidally propagating in the direction of plasma current (co-direction). In addition to the  $n = 5$  mode at  $f_L \sim 90$  kHz, three other modes are detected during NBI: an  $n = -1$  mode at  $f_L \sim 65$  kHz, an  $n = 4$  mode at  $f_L \sim 150$  kHz, and an  $n = 10$  mode at  $f_L \sim 180$  kHz. Evidence for weaker modes at other mode numbers is also visible just above the broadband fluctuation level. The modes below 30 kHz correspond to the global current-driven tearing modes. Comparison of the NBI-off and NBI-on spectra, as shown in Figs. 6(a) and 6(b), indicates that these coherent high-frequency ( $>50$  kHz) modes are only observed in the NBI-heated plasmas, clearly establishing the fast-ion driving mechanism. Previously, it was shown that the  $n = 4$  frequency linearly depends on the Alfvén velocity but also remains well below the calculated  $n = 4$  TAE gap at 200–300 kHz.<sup>13</sup> In addition, earlier studies also revealed strong three-wave coupling among the  $n = 5$ ,  $n = -1$ , and  $n = 4$  modes. The possibility that the  $n = -1$  mode is

nonlinearly generated was speculated.<sup>14</sup> Later in Sec. V, other possibilities will be discussed.

One important property of EP-instabilities is their radial structure. A multi-chord interferometer is used to measure the spatial structure of line-integrated electron density fluctuations ( $\int \tilde{n}_e dl$ ). Figure 7(a) shows the power distribution of  $\int \tilde{n}_e dl$  in the plane of frequency and major radius ( $R - R_{mag}$ ), where  $R_{mag} = 1.54$  m is the location of the magnetic axis. The frequency is evaluated in the plasma frame where the Doppler shift due to the plasma rotation has been removed. The corresponding Alfvén continuum frequency ( $k_{||} v_A / 2\pi$ ) at the mid-plane ( $Z = 0$ ) along the major radius is also plotted. Strongest density fluctuations are observed near the core where fast ions reside. As shown in Fig. 7(a), the  $m = 1$ ,  $n = 5$  density fluctuation peaks near  $R - R_{mag} \sim -0.1$  m and  $f_p \sim 65$  kHz, while the  $m = 1$ ,  $n = 4$  density fluctuation peaks near  $R - R_{mag} \sim 0.05$  m and  $f_p \sim 130$  kHz. The locations of these peaks lie in the vicinity of their corresponding Alfvén continuum. Figures 7(b)–7(d) correspond to the  $n = 4$  and  $n = 5$  EP density fluctuations for different beam and plasma species and will be discussed in Sec. IV D. The density fluctuation of  $n = -1$  is shown in Fig. 8, where the

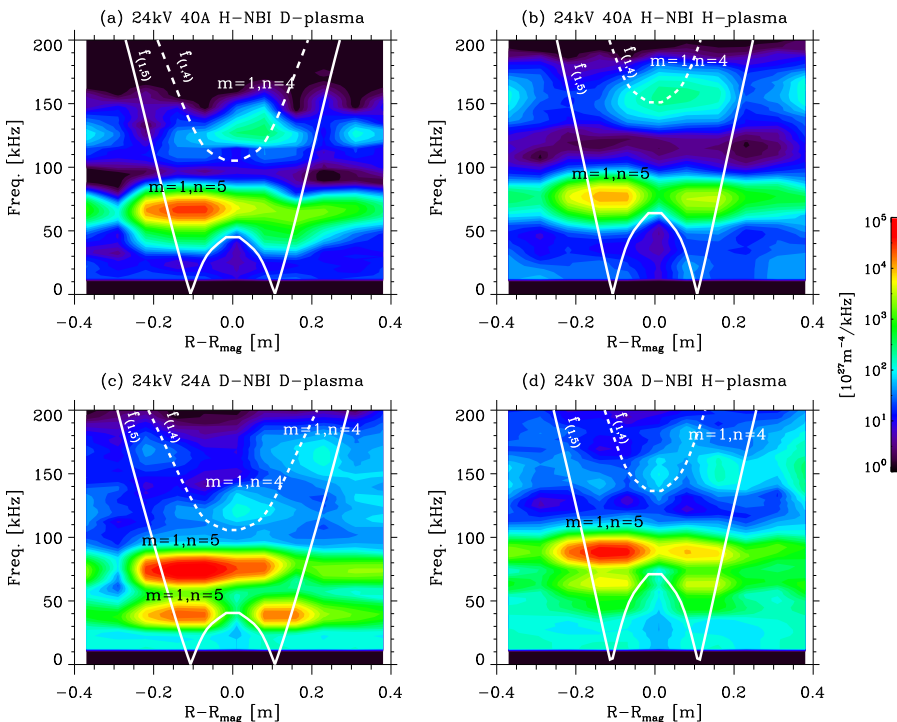


FIG. 7. Spatial and frequency (in the plasma frame) distribution of line-integrated electron density fluctuation ( $\int \tilde{n}_e dl$ ) power for the  $n = 4$  and  $n = 5$  EP modes with: (a) 40 A H-beam into D-plasma, (b) 40 A H-beam into H-plasma, (c) 24 A D-beam into D-plasma, (d) 30 A D-beam into H-plasma. In each case, a 24 kV beam is injected into discharges with  $I_\phi \sim 300$  kA,  $\bar{n}_e \sim 0.7 \times 10^{19} \text{ m}^{-3}$ , edge  $q_a = 0$ , and  $R_{mag} = 1.54$  m. The Alfvén continua ( $f = k_{||} v_A / 2\pi$ ) at the mid-plane are over plotted: solid line for  $m = 1$ ,  $n = 5$  and dashed line for  $m = 1$ ,  $n = 4$ .

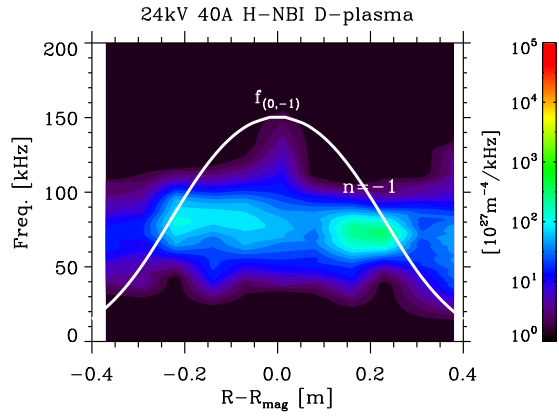


FIG. 8. Spatial and frequency (in the plasma frame) distribution of line-integrated electron density fluctuation ( $\int \tilde{n}_e dl$ ) power for the  $n = -1$  EP mode, where  $R_{mag} = 1.54$  m. The Alfvén continuum ( $f = k_{||} v_A / 2\pi$ ) at the mid-plane for  $m = 0$ ,  $n = -1$  is over plotted. Data are for discharges where a 24 kV H-beam is injected into a deuterium plasma with  $I_\phi \sim 300$  kA,  $\bar{n}_e \sim 0.7 \times 10^{19} \text{ m}^{-3}$ , and edge  $q_a = 0$ .

peaking location is  $R - R_{mag} \sim 0.2$  m and  $f_p \sim 70$  kHz is also close to the  $m = 0$ ,  $n = -1$  Alfvén continuum. This feature is similar to the property of the energetic particle continuum modes, whose frequency tends to be near the Alfvén continuum.<sup>37</sup> Density fluctuations associated with EP modes exhibit a strong inboard-outboard asymmetry:  $n = 5$  peaks inboard while  $n = 4$  and  $n = -1$  peaks outboard. Considering the substantial Larmor radius of fast ions ( $r_L \sim 0.04$  m and  $r_L/a \sim 0.1$ ) due to the weak magnetic field, one possible explanation is that the fast-ion density is not constant on the same magnetic flux surface, leading to asymmetric drive of EP instabilities. A detailed explanation remains to be explored. Future efforts of detecting electron temperature fluctuations with a high-repetition-rate Thomson scattering<sup>38</sup> or local density and electric potential fluctuations with a heavy ion beam probe<sup>39</sup> may provide critical information.

The resonance condition [Eq. (7)] can be satisfied for the  $m = 1$ ,  $n = 5$  mode. For fast H-ions with energy 24 kV and velocity pitch  $v_{||}/v = 0.9$  launched at  $R - R_{mag} = -0.1$  m and  $Z = 0$ , orbit calculations in the equilibrium magnetic field give a toroidal transit frequency  $f_\phi \sim 185$  kHz. Consider  $l = 0$  resonance in Eq. (7),

$$q_{fi} \approx \frac{m}{n - f/f_\phi}. \quad (13)$$

Plugging in  $m = 1$ ,  $n = 5$ , and  $f = 65$  kHz leads to  $q_{fi} \approx 0.215$ , which resides inside the plasma (Fig. 3). Considering uncertainty in the fast-ion velocity pitch and the mode location, we conclude that the resonance condition can be satisfied.

## B. Dependence on beam and plasma species

Energetic particle instabilities can be excited by the free energy available in the gradients of the fast-ion distribution function in real or phase (velocity) space. To unfold the driving mechanism, it is revealing to investigate the dependence of the EP-mode characteristics (frequency, amplitude, and spatial

structure) on the ratio of the beam velocity ( $v_B$ ) to the Alfvén velocity ( $v_A$ ). Our experiments involve four types of plasmas with the same toroidal current  $I_\phi \sim 300$  kA and similar central line-averaged electron density  $\bar{n}_e \sim 0.7 \times 10^{19} \text{ m}^{-3}$ , in an attempt to reduce the complication from density and magnetic field variations. The Alfvén velocity ( $v_A = B/\sqrt{\mu_0 n_i m_i}$ ) is varied by switching plasma species from D to H, while the beam-ion velocity ( $v_B = \sqrt{2E/m_B}$ ) is varied by changing the NBI gas fuel from H to D. As shown in Fig. 9(a), this approach covers both super-Alfvénic ( $v_B/v_{A0} > 1$ ) and sub-Alfvénic ( $v_B/v_{A0} < 1$ ) fast-ions, where  $v_{A0}$  is the Alfvén velocity at the plasma center.

EP instabilities are excited as  $v_B/v_{A0}$  varies from super- to sub-Alfvénic, implying that the driving mechanism lies in the real space gradient instead of the velocity space. Furthermore, the  $n = 5$ ,  $n = 4$ , and  $n = -1$  modes remain as the dominant EP instabilities as beam and plasma species vary. Figure 9(b) summarizes the frequency power spectra (in the plasma frame) of the  $n = 5$  and  $n = 4$  poloidal magnetic fluctuations ( $\tilde{b}_\theta$ ) from edge coils. The magnetic spectra of the  $n = 5$  mode exhibit stronger dependence on the fast-ion species than the plasma species. Multiple frequency peaks are observed in the D-beam cases: two peaks (40 kHz and 74 kHz) in the D-beam into D-plasma and three peaks

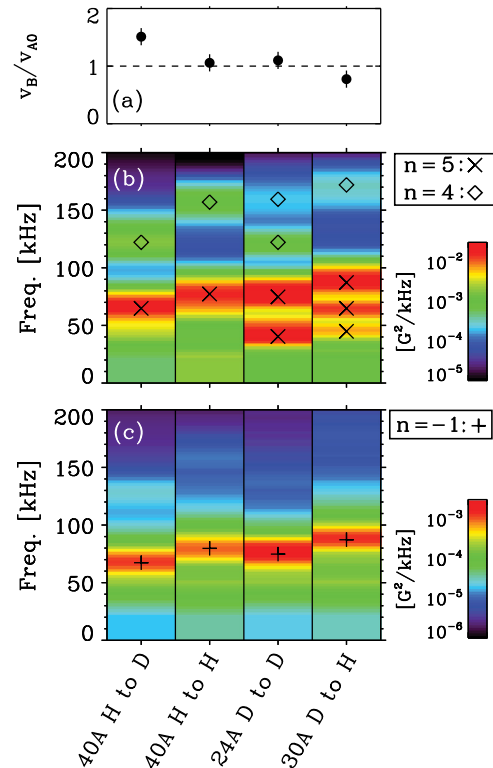


FIG. 9. Plasma and beam species dependence of (a) ratio of beam velocity to core Alfvén velocity ( $v_B/v_{A0}$ ), (b) sum of edge poloidal magnetic fluctuation frequency spectra for  $n = 5$  and  $n = 4$  EP modes, (c) frequency spectra of the  $n = -1$  EP mode for cases: 40 A H-beam into D-plasma (H to D), 40 A H-beam into H-plasma (H to H), 24 A D-beam into D-plasma (D to D), and 30 A D-beam into H-plasma (D to H). The frequency spectra are in the plasma frame. Symbols mark the frequency peaks: ( $\times$ ) cross for  $n = 5$ , diamond for  $n = 4$ , and (+) for  $n = -1$ . For all four cases, the beam at 24 kV is injected into discharges with  $I_\phi \sim 300$  kA,  $\bar{n}_e \sim 0.7 \times 10^{19} \text{ m}^{-3}$ , and edge safety factor  $q_a = 0$ .

(45 kHz, 65 kHz, and 87 kHz) in the D-beam into H-plasma. In contrast, only one frequency peak dominates in the H-beam cases: 65 kHz in the H-beam into D-plasma and 77 kHz in the H-beam into H-plasma.

The  $n = 5$  frequency shows weak dependence on  $v_{A0}$ , consistent with previous frequency-scaling studies.<sup>13</sup> In the H-beam cases, switching from D-plasma to H-plasma increases  $v_{A0}$  by 42%, while the  $n = 5$  frequency only increases by 18% (from 65 kHz to 77 kHz). Similar weak dependence of the  $n = 5$  frequency on  $v_{A0}$  is observed in the D-beam cases. On the contrary, the  $n = 4$  frequency [Fig. 9(b)] shows strong dependence on  $v_{A0}$  (roughly  $f^{n=4} \propto v_{A0}$ ) while only weak dependence on  $v_B$ . The  $n = -1$  frequency [Fig. 9(c)] exhibits weak dependence on  $v_{A0}$  and  $v_B$ .

The spatial structures of line-integrated density from the multi-chord interferometer as  $v_B/v_{A0}$  varies are summarized in Fig. 7. Interestingly, the density fluctuations associated with the  $n = 4$  and  $n = 5$  always peak near their corresponding Alfvén continuum. In addition, these density fluctuations always exhibit asymmetry along the major radius, where  $n = 5$  peaks inboard while  $n = 4$  peaks outboard. The  $n = -1$  density fluctuations also peak near the  $m = 0$ ,  $n = -1$  Alfvén continuum. Due to the similarities, only one case is shown in Fig. 8.

In addition to the amplitude profile, the relative phase profile of the strongest  $n = 5$  density fluctuation ( $\int \tilde{n}_e dl$ ) is resolved using fluctuation cross-correlation analysis. The spatial profiles obtained after integrating over their corresponding frequency band, along with equilibrium density ( $\int n_e dl$ ) profiles, are shown in Fig. 10. For the cases with multiple  $n = 5$  modes at different frequencies, the integration frequency includes all the modes, as their spatial structures are similar, as shown in Fig. 7. For all cases, the rms-amplitude of  $\int \tilde{n}_e dl$  is stronger in the inboard side ( $R - R_{mag} < 0$ ) and peaks near  $R - R_{mag} \sim -0.1$  m. The phase profiles exhibit  $\sim \pi$  shift across the magnetic axis, roughly consistent with the  $m = 1$  nature determined from edge magnetic coils. Furthermore, another  $\pi$  shift occurs  $\sim 0.25$  m away from the magnetic axis. The potential exists for the presence of higher poloidal harmonics, as in the tokamak,<sup>40,41</sup> but theoretical modeling and more detailed measurements are required to pursue this possibility.

The density fluctuation level can be estimated using the maximum rms-amplitude of  $\int \tilde{n}_e dl$  normalized by equilibrium  $\int n_e dl$  from the same chord, i.e.,

$$\left(\frac{\tilde{n}_e}{n_e}\right)_{est.} \equiv \frac{\max\left[\left(\int \tilde{n}_e dl\right)_{rms}\right]}{\int n_e dl}. \quad (14)$$

Figure 11 shows the relative density fluctuation level using Eq. (14) and edge poloidal magnetic fluctuation level ( $\tilde{b}_{\theta,rms}/B_0$ ) at  $r \sim a$  for the  $n = 5$  EP mode as plasma and beam species vary. The relative density fluctuation level ranges from 0.3% to 0.5% and remains  $6\times$  the corresponding edge magnetic fluctuation level. The constant ratio of internal ( $\int \tilde{n}_e dl$ ) to edge ( $\tilde{b}_{\theta}$ ) implies weak dependence of EP mode structure on plasma and beam species variations. The D-beam drives larger fluctuations than the H-beam in both H- and D-plasmas, implying more free energy or more

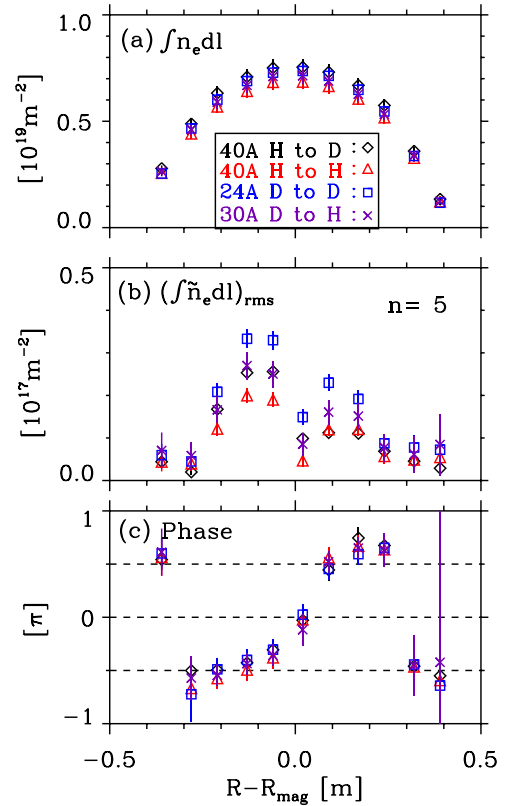


FIG. 10. Profiles of (a) equilibrium of line-integrated electron density ( $\int n_e dl$ ), (b) fluctuation rms-amplitude, and (c) relative phase of line-integrated electron density fluctuations ( $\int \tilde{n}_e dl$ ) associated with the  $n = 5$  EP mode for: 40 A H-beam into D-plasma (H to D), 40 A H-beam into H-plasma (H to H), 24 A D-beam into D-plasma (D to D), and 30 A D-beam into H-plasma (D to H). In each case, the beam at 24 kV is injected into discharges with  $I_\phi \sim 300$  kA, edge safety factor  $q_a = 0$ , and  $R_{mag} = 1.54$  m.

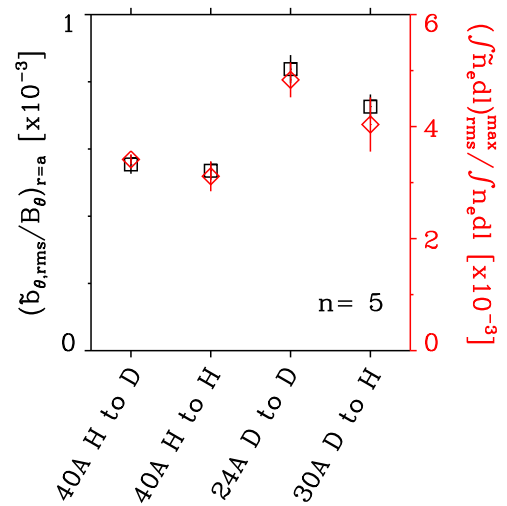


FIG. 11. Relative density fluctuation level (red diamond) estimated from Eq. (14),  $\max\left[\left(\int \tilde{n}_e dl\right)_{rms}\right]/\int n_e dl$ , and the relative edge poloidal magnetic fluctuation level (black square),  $\tilde{b}_{\theta,rms}/B_0$ , for the  $n = 5$  EP mode for: 40 A H-beam into D-plasma (H to D), 40 A H-beam into H-plasma (H to H), 24 A D-beam into D-plasma (D to D), and 30 A D-beam into H-plasma (D to H). In each case, the neutral beam at 24 kV is injected into discharges with  $I_\phi \sim 300$  kA, and edge safety factor  $q_a = 0$ .

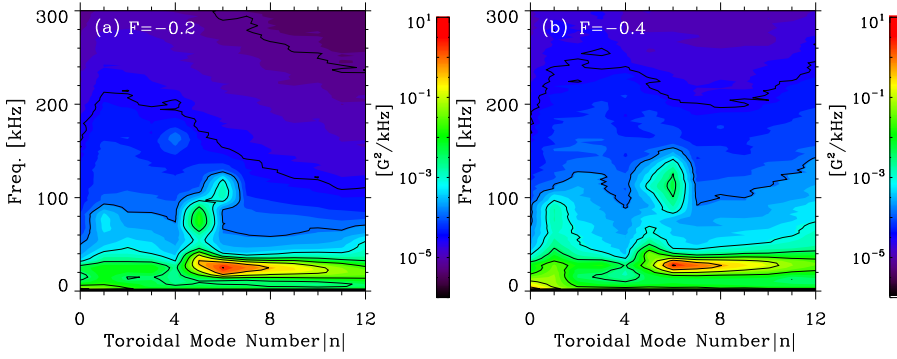


FIG. 12. Frequency (in the lab frame) variation with toroidal mode number spectra ( $|n|$ ) of poloidal magnetic fluctuations for 40 A H-beams at 24 kV injected into D plasmas with (a)  $F = -0.2$  and (b)  $F = -0.4$ , where  $I_\phi \sim 300$  kA and  $\bar{n}_e \sim 0.7 \times 10^{19} \text{ m}^{-3}$ .

efficient wave-particle energy transfer from the D fast ions. TRANSP modeling does not reveal significant difference in the distribution functions of D and H fast ions. As shown in Fig. 3, the D fast-ions lead to larger  $q_{fi}$  than the H fast-ions. As the fast-ion safety factor describes the resonance condition between fast ions and MHD instabilities,  $q_{fi}^D > q_{fi}^H$  suggests higher probability of wave-particle resonance for the D fast ions, which may serve to excite stronger instabilities. For the same beam ions, fluctuations in H-plasmas tend to be slightly weaker than in D-plasmas. In particular, for the D-beam cases, larger fluctuations occur in the D-plasma than in the H-plasma, in spite of the lower beam current (24 A vs. 30 A). This suggests larger damping in H-plasma with larger  $v_A$ .

### C. Dependence on safety factor

In addition to  $v_A$  and  $v_B$ , the safety factor  $q$  is another important parameter in EP physics, as it affects not only continuum damping from bulk plasmas but also wave-particle resonance condition. To investigate the impact of  $q$  profile on observed EP instabilities, H-beam (40 A and 24 kV) is injected into a series of D-plasmas with the  $F$  value gradually decreasing from 0 to  $-0.4$  while keeping  $I_\phi \sim 300$  kA and  $\bar{n}_e \sim 0.7 \times 10^{19} \text{ m}^{-3}$ . As shown in Fig. 1(a), the  $q$  value across the whole minor radius gradually decreases as  $F$  decreases. The local electron density profile [Fig. 1(b)] reconstructed from equilibrium interferometry measurements does not exhibit pronounced variation with  $F$  and remains flat with small radial gradient inside  $r/a \sim 0.5$ , the region where the strong EP-mode density fluctuations are detected. One noticeable difference is that the electron density near  $r/a \sim 0.6$  gets more peaked as  $F$  decreases.

The strongest EP instability transits from  $n = 5$  to  $n = 6$  as  $F$  decreases. Figure 12 shows the  $f$  vs.  $n$  power spectra of poloidal magnetic fluctuations from the plasmas with  $F = -0.2$  and  $F = -0.4$ . Comparison with the  $F = 0$  case [Fig. 6(b)] shows that the toroidal mode number of the dominant EP-mode transits from  $n = 5$  to  $n = 6$  as  $F$  decreases from 0.0 to  $-0.4$ , while the poloidal mode number remains  $m = 1$ . The mode frequency always resides well below the predicted TAE frequency [Fig. 4(b)]. The strongest resonant tearing mode also transits from  $n = 5$  to  $n = 6$  as  $q_0$  drops below 0.2. However, the  $n$ -transition of EP modes occurs at more negative  $F$ -value. As shown in Fig. 12(b),  $n = 6$  becomes the strongest resonant tearing mode at  $F = -0.2$ , while  $n = 5$  remains the strongest EP mode and  $n = 6$  just becomes visible. Consequently, a more negative  $F$ -value (or

smaller  $q_0$ ) is required for the  $n$ -transition of the EP-mode than that of the tearing modes. This difference may arise from the difference between fast-ion safety factor ( $q_{fi}$ ) and MHD safety factor ( $q$ ), as  $q_{fi}$  describes the wave-particle resonance and  $q$  governs the MHD-mode resonance.

Figure 13(a) shows the reduction of  $q_{fi}^H$  and  $q_0$  as  $F$  decreases, where  $q_{fi}^H$  is calculated at  $r = 0.1$  m (peak location of the  $n = 5$  density fluctuation) for H-ion with energy 24 kV and velocity pitch 0.9 (values from TRANSP modeling). The  $n$ -transition of EP modes is illustrated in Fig. 13(b). The  $n = 5$  frequency decreases  $\sim 10$  kHz as  $F$  is reduced, which may be associated with equilibrium changes as reported for tokamak plasmas.<sup>42</sup> The transition from  $n = 5$  to  $n = 6$  occurs between  $F = -0.2$  and  $-0.3$  when  $q_{fi}^H$  drops below  $\sim 0.215$ . The mode frequency also increases  $\sim 20$  kHz after the transition. Interestingly, earlier calculations (Sec. IV A) with Eq. (13) show that  $q_{fi}^H \approx 0.215$  is required to meet wave-particle resonance condition for the  $m = 1, n = 5$  mode at the measured frequency. As  $q_{fi}^H$  is reduced below 0.215, the resonance condition for the  $m = 1, n = 5$  mode is violated. However, the resonance condition for the  $m = 1, n = 6$  mode is still satisfied, as it only requires  $q_{fi}^H \approx 0.18$ .

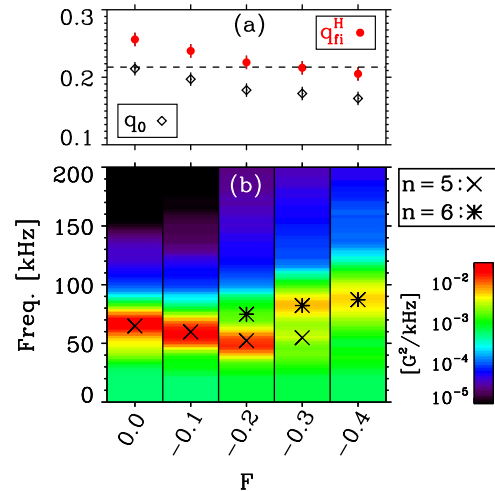


FIG. 13. Reversal parameter  $F$  dependence of (a) magnetic safety factor  $q$  (black diamond) at  $r = 0$  and fast-ion  $q_{fi}^H$  (red dot) at  $r = 0.1$  m-calculated for H-ion with energy 24 kV and velocity pitch 0.9, where the horizontal dashed line corresponds to the  $m = 1, n = 5$  wave-particle resonance condition,  $q_{fi}^H \approx 0.215$ , (b) sum of edge-poloidal-magnetic fluctuation frequency spectra (in the plasma frame) of the  $n = 5$  and  $n = 6$  EP modes. Symbols mark the frequency peaks: ( $\times$  cross) for  $n = 5$  and ( $*$  star) for  $n = 6$ . Data are for H-beam (40 A and 24 kV) injection into D plasmas ( $I_\phi \sim 300$  kA and  $\bar{n}_e \sim 0.7 \times 10^{19} \text{ m}^{-3}$ ).

Electron density fluctuations associated with the  $n = 6$  EP mode are also strongly core-localized. As shown in Fig. 14, the rms-amplitude of  $\int \tilde{n}_e dl$  peaks near  $R - R_{mag} \sim -0.15$  m and exhibits a strong inboard and outboard asymmetry, as did the  $n = 5$  mode. Furthermore, the peak location lies near the  $m = 1, n = 6$  Alfvén continuum, again similar to the  $n = 5$  mode shown in Fig. 7.

The  $F$ -scan experiments with D-fast ions confirm the connection between toroidal mode transition and wave-particle resonance condition. Figure 15(a) shows the reduction of  $q_{fi}^D$  and  $q_0$  as  $F$  decreases, where  $q_{fi}^D$  is calculated at  $r = 0.1$  m for D-ion with energy 24 kV and velocity pitch 0.9. Compared to H ion, the  $m = 1, n = 5$  wave-particle resonance condition for D ion [Eq. (13)] slightly increases,  $q_{fi}^D \approx 0.22$  vs.  $q_{fi}^H \approx 0.215$ . As shown in Fig. 3, the fast-ion safety factor exhibits a species dependence,  $q_{fi}^D > q_{fi}^H$ . Consequently,  $q_{fi}^D$  in Fig. 15(a) remains above 0.22 as  $F$  decreases. Hence, the resonance condition for the  $m = 1, n = 5$  mode remains to be satisfied as  $F$  decreases. This is consistent with the EP-mode measurements in Fig. 15(b). In contrast to the H-beam case,  $n = 5$  remains as the dominant EP mode as  $F$  decreases during the D-beam injection, while the  $n = 6$  mode only becomes visible at  $F = -0.4$ .

To investigate the variation of different fluctuation fields and mode structure as  $F$  and  $q$  change, we compare the internal density fluctuation level [defined in Eq. (14)] with the edge poloidal magnetic fluctuation level, as shown in Fig. 16. The  $n = 5$  internal density fluctuation decreases faster with reduced  $q$  than the edge magnetic fluctuation. Furthermore, as shown in Figs. 6 and 14, the density fluctuation associated with the  $n = 6$  mode peaks slightly outward (larger  $|R - R_{mag}|$ ) than that of the  $n = 5$  mode. Overall, the  $n = 6$  fluctuation level for  $F \leq -0.3$  is weaker than  $n = 5$  at  $F = 0$ . Comparison of Alfvén continua for  $F = 0$  and  $F = -0.4$  in Fig. 4 reveals more continuum damping near the edge as  $F$  reduces, primarily caused by the  $q = 0$  surface residing inside the plasma, which may contribute to the reduced fluctuation level.

## D. Temporal dynamics of EP instabilities

The detailed temporal evolution of the dominant EP-mode amplitude is resolved after averaging over 1000

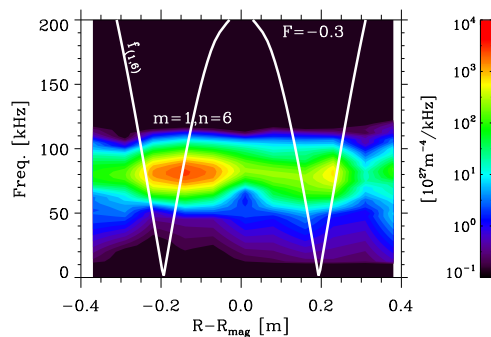


FIG. 14. Spatial and frequency (in the plasma frame) distribution of line-integrated electron density fluctuation ( $\int \tilde{n}_e dl$ ) power for the  $n = 6$  EP mode, where  $R_{mag} = 1.54$  m. The Alfvén continuum ( $f = k_{||} v_A / 2\pi$ ) at the mid-plane for  $m = 1, n = 6$  is over plotted. Data are for H-beam (40 A and 24 kV) injection into D-plasma ( $I_\phi \sim 300$  kA,  $\bar{n}_e \sim 0.7 \times 10^{19} \text{ m}^{-3}$ ,  $F = -0.3$ , and  $q_a = -0.056$ ).

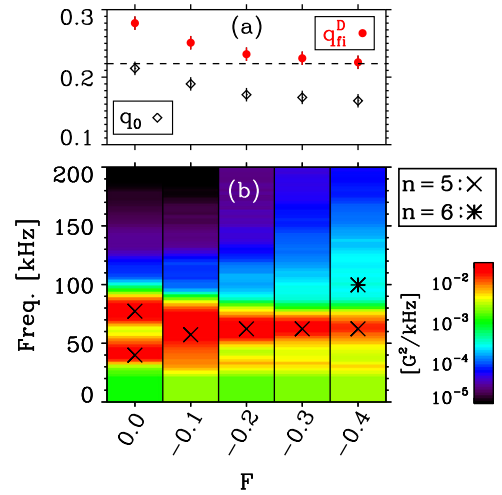


FIG. 15. Reversal parameter  $F$  dependence of (a) magnetic safety factor  $q$  (black diamond) at  $r = 0$  and fast-ion  $q_{fi}^D$  (red dot) at  $r = 0.1$  m calculated for D-ion with energy 24 kV and velocity pitch 0.9, where the horizontal dashed line corresponds to the  $m = 1, n = 5$  wave-particle resonance condition,  $q_{fi}^D \approx 0.22$ , (b) sum of edge-poloidal-magnetic fluctuation frequency spectra (in the plasma frame) of the  $n = 5$  and  $n = 6$  EP modes. Symbols mark the frequency peaks: ( $\times$  cross) for  $n = 5$  and ( $*$  star) for  $n = 6$ . Data are for D-beam (24 A and 24 kV) injection into D plasmas ( $I_\phi \sim 300$  kA and  $\bar{n}_e \sim 0.7 \times 10^{19} \text{ m}^{-3}$ ).

similar bursts using the peak of the  $n = 5$  mode as the time marker. The temporal evolutions of edge poloidal magnetic fluctuations for three dominant EP-modes ( $\tilde{b}_{\theta,rms}^{n=5}, \tilde{b}_{\theta,rms}^{n=4}$ , and  $\tilde{b}_{\theta,rms}^{n=-1}$ ) are shown in Fig. 17(a), where  $\tilde{b}_{\theta,rms}^{n=5}$  not only has a larger amplitude than  $\tilde{b}_{\theta,rms}^{n=4}$  and  $\tilde{b}_{\theta,rms}^{n=-1}$  but also occurs earlier in time. To quantify temporal dynamics of the EP modes, exponential growth and decay functions are used to fit the time evolution of  $\tilde{b}_{\theta,rms}^n$ , i.e.,

$$b_{\theta,rms} \propto e^{\gamma t} \text{ or } b_{\theta,rms} \propto e^{-\gamma t}. \quad (15)$$

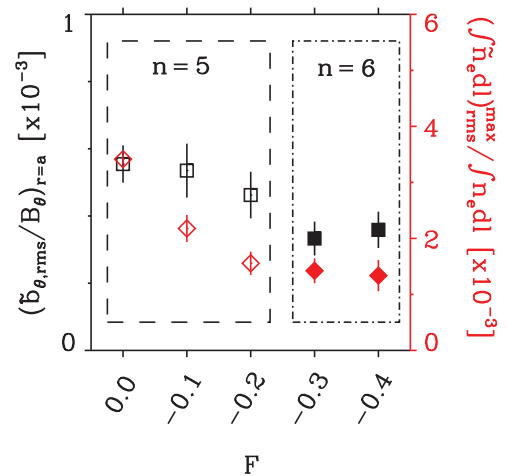


FIG. 16. Relative density fluctuation level (red diamond) estimated from Eq. (14),  $\max[\int \tilde{n}_e dl]_{rms} / \int \tilde{n}_e dl$ , and relative edge poloidal magnetic fluctuation level (black square), for the  $n = 5$  (open symbol) and  $n = 6$  (solid symbol) EP modes at various reversal parameters ( $F$ ). Data are for H-beam (40 A and 24 kV) injection into D plasmas ( $I_\phi \sim 300$  kA and  $\bar{n}_e \sim 0.7 \times 10^{19} \text{ m}^{-3}$ ). As the mode transits from  $n = 5$  to  $n = 6$ , the ratio of the density fluctuation level to the edge magnetic fluctuation level drops from 6 to 4.

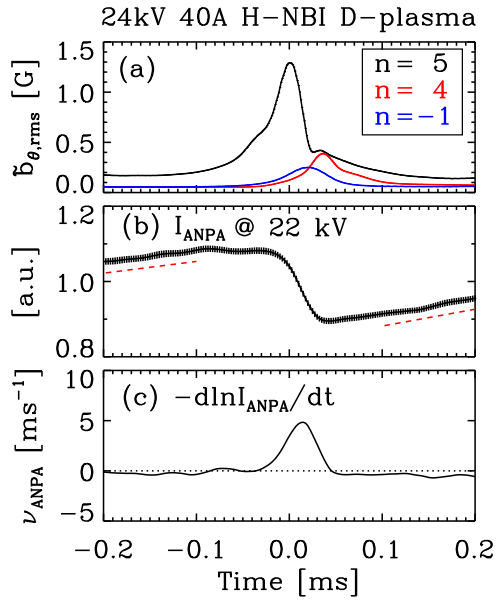


FIG. 17. Time traces of (a) rms-amplitudes of edge poloidal magnetic fluctuations ( $\tilde{b}_{\theta,rms}$ ) for the  $n = 5$ ,  $n = 4$ , and  $n = -1$  EP modes; (b) the ANPA signal ( $I_{ANPA}$ ) at the energy 22 kV; (c) the instantaneous decay rate of the ANPA signal defined as  $\nu_{ANPA} = -(d \ln I_{ANPA} / dt)$ . Data are for H-beam (24 kV and 40 A) injected into deuterium plasmas with  $I_{\phi} \sim 300$  kA,  $\bar{n}_e \sim 0.7 \times 10^{19} \text{ m}^{-3}$ , and edge  $q_a \sim 0$ .

For the  $n = 5$  mode,  $\tilde{b}_{\theta,rms}^{n=5}$  increases with a growth rate  $\gamma_L^{n=5} \sim 35 \pm 3 \text{ ms}^{-1}$  before reaching its maximum value. The decay of  $\tilde{b}_{\theta,rms}^{n=5}$  after  $t = 0$  proceeds in two stages: faster decay with  $\gamma_{D,F}^{n=5} \sim 85 \pm 10 \text{ ms}^{-1}$  until  $t = 0.03 \text{ ms}$  and slower decay with  $\gamma_{D,S}^{n=5} \sim 28 \pm 2 \text{ ms}^{-1}$  after  $t = 0.03 \text{ ms}$ . Interestingly, the transition of  $\tilde{b}_{\theta,rms}^{n=5}$  from faster to slower decay ( $\gamma_{D,S}^{n=5}$ ) occurs approximately when  $\tilde{b}_{\theta,rms}^{n=4}$  reaches its maximum value. Previous studies noted strong three-wave coupling among the  $n = 5$ ,  $n = 4$ , and  $n = -1$  modes.<sup>14</sup> This nonlinear wave-wave interaction may induce mode energy transfer from  $n = 5$  to  $n = 4$  as  $\tilde{b}_{\theta,rms}^{n=4}$  increases, thereby enhancing the energy loss of the  $n = 5$  mode and increasing the damping rate. The temporal dynamics of the  $n = 4$  and  $n = -1$  are less complicated:  $\tilde{b}_{\theta,rms}^{n=4}$  evolves with a growth rate  $\gamma_L^{n=4} \sim 50 \pm 5 \text{ ms}^{-1}$  and  $\gamma_D^{n=4} \sim 35 \pm 5 \text{ ms}^{-1}$ , while  $\tilde{b}_{\theta,rms}^{n=-1}$  grows with the rate of  $\gamma_L^{n=-1} \sim 40 \pm 3 \text{ ms}^{-1}$  and decays with the rate of  $\gamma_D^{n=-1} \sim 48 \pm 4 \text{ ms}^{-1}$ . Interestingly, the decay rate decreases as  $n$  increases,  $\gamma_D^{n=-1} > \gamma_D^{n=4} > \gamma_D^{n=5}$ . This trend is consistent with the continuum damping calculated for the DIII-D experiments,<sup>43</sup> which decreases as  $n$  increases. The damping mechanism in a RFP remains to be explored.

## E. Fast ion measurements

Fast-ion transport correlated with the EP modes is measured with the ANPA diagnostic. As shown in Fig. 17(b), the tangential-view ANPA signal at 22 kV (near the beam energy 24 kV) contains a slow-growth phase arising from the beam fueling followed by a rapid drop ( $\sim 15\%$  decrease in less than 0.04 ms) when the EP modes peak. The measured

fast-neutral flux ( $I_{ANPA}$ ) is primarily from fast ions charge-exchanging with background neutrals. Furthermore, less than 1% variation of the  $D_{\alpha}$  emission measurements indicates no significant change in the background neutral density. Hence, the  $I_{ANPA}$  decrease is likely a consequence of fast ions being scattered by the excited instabilities.

The fast time response of the ANPA diagnostic provides important information on fast-ion transport during the EP modes. To quantify the temporal dynamics of  $I_{ANPA}$ , an instantaneous decay rate is defined as

$$\nu_{ANPA} = -\frac{1}{I_{ANPA}} \frac{dI_{ANPA}}{dt}, \quad (16)$$

where  $\nu_{ANPA}$  is assumed to be governed by the continuous fueling rate ( $\nu_{fuel}$ ) from the beam injection and the loss-rate ( $\nu_{loss}$ ) due to the excited instabilities, i.e.,

$$-\nu_{ANPA} = \nu_{fuel} - \nu_{loss}. \quad (17)$$

The fueling rate  $\nu_{fuel}$  remains constant throughout due to the constant beam injection. As shown in Fig. 17(b), away from the EP modes ( $t < -0.1 \text{ ms}$  and  $t > 0.1 \text{ ms}$ ),  $I_{ANPA}$  gradually increases with  $\nu_{ANPA} \sim -0.4 \pm 0.1 \text{ ms}^{-1}$  and  $\nu_{loss} \sim 0$  as no modes are excited; thus, the constant fueling rate can be determined as  $\nu_{fuel} \sim 0.4 \pm 0.1 \text{ ms}^{-1}$  at the maximum beam current (40 A). If no EP instabilities excited, it takes  $\sim 2.5 \pm 0.7 \text{ ms}$  for  $I_{ANPA}$  to linearly increase from 0 to the averaged value  $\bar{I}_{ANPA} = 1$ . Recall, initial onset of the NBI-driven modes occurs  $2.5 \pm 0.5 \text{ ms}$  after NBI turn-on, as shown in Fig. 5. With the excitation of the EP modes, a stiff fast-ion density profile is clamped near the point of marginal instability. This process resembles a classical predator-prey relaxation oscillation, where the EP instabilities act as the predator that preys upon fast ions. This phenomenon has also been observed on beam-driven instabilities in tokamaks.<sup>44</sup>

The instantaneous ANPA decay rate ( $\nu_{ANPA}$ ) is shown in Fig. 17(c) and reaches maximum at  $t \sim 0.015 \text{ ms}$ . Combining  $\nu_{ANPA}$  and  $\nu_{fuel} \sim 0.4 \text{ ms}^{-1}$ , the instantaneous loss rate is ready to be calculated via  $\nu_{loss} = \nu_{fuel} + \nu_{ANPA}$ . Figure 18 shows the dependence of  $\nu_{loss}$  on the magnetic fluctuations summed over the three dominant EP-modes. Before  $t \leq -0.003 \text{ ms}$ , the  $n = 5$  mode is the dominant mode and  $\nu_{loss} \propto \tilde{b}_{\theta}^{2.2 \pm 0.4}$ . After  $t > -0.003 \text{ ms}$ ,  $\nu_{loss}$  is greatly enhanced when the  $n = 4$  and  $n = -1$  modes are excited to a significant level. Multiple modes with different spatial structures (Figs. 7 and 8) provide wave-particle resonance over a larger region, resulting in stronger fast-ion transport.

## V. SUMMARY AND DISCUSSION

Multiple energetic-particle instabilities are observed during 1 MW tangential neutral-beam injection in a RFP. This article reports on experimental investigation of these EP-modes, including the dependence of mode characteristics (frequency, wavenumber, amplitude, and internal structure) on plasma/fast-ion species and safety factor profiles. When switching beam ions from hydrogen to deuterium, the dominant  $m = 1$ ,  $n = 5$  mode splits into multiple frequencies with an increased fluctuation level. Furthermore, as the safety

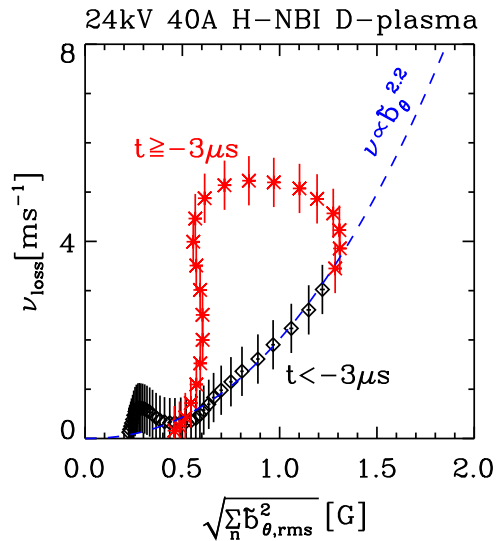


FIG. 18. Instantaneous fast-ion loss rate inferred from the ANPA signal vs. edge poloidal magnetic fluctuations ( $\sqrt{\sum_n b_\theta^2}$ ) summed over the  $n = 5$ ,  $n = 4$ , and  $n = -1$  EP modes. Data are for H-beam (24 kV and 40 A) injection into deuterium plasmas with  $I_\phi \sim 300$  kA,  $\bar{n}_e \sim 0.7 \times 10^{19} \text{ m}^{-3}$ , and edge  $q_a = 0$ .

factor ( $q$ ) decreases, the toroidal mode number of the dominant mode transits from  $n = 5$  to  $n = 6$  while retaining the same poloidal mode number  $m = 1$ . The transition occurs when the wave-particle resonance condition for the  $m = 1$ ,  $n = 5$  mode cannot be satisfied at the measured frequency. Presumably, the  $n = 6$  mode is destabilized as the fast-ion distribution further evolves without the impact of fast-ion transport due to the  $n = 5$  mode. Density fluctuations associated with these EP instabilities peak near the core where fast ions reside and exhibit a strong inboard-outboard asymmetry. Furthermore, the measured mode frequency is close to the corresponding shear Alfvén wave frequency. Fast-ion measurements show that mode-particle interactions resemble the classical predator-prey relaxation oscillations. Fluctuation-induced particle transport and continuous beam fueling lead to a stiff and marginally stable fast-ion density profile. The temporal fast-ion dynamics also reveals enhanced fast-ion transport with the onset of multiple modes.

When considering the different spatial structure (Fig. 7) and time history in the occurrence of multiple EP modes (Fig. 17), one possible excitation sequence is speculated in Fig. 19. By tapping the free energy residing in the steep fast-ion density profile (Fig. 2), the  $n = 5$  mode is destabilized around  $r = 0.1$  m. The strong interaction between fast ions and the excited  $n = 5$  mode leads to a local flattening of fast-ion density profile near  $r = 0.1$  m. This relaxation process steepens the density profile near the boundary of the flattening region. The enhanced fast-ion density gradient (at the boundary) drives the  $n = 4$  mode near  $r = 0.05$  m and the  $n = -1$  mode near  $r = 0.18$  m. This process is similar to the hole-clump creation in the phase space.<sup>45,46</sup> Double-resonant fast particle-wave interactions<sup>47</sup> found in numerical EP simulations of the ASDEX Upgrade discharges may also be relevant to our experiments. Future experiments with the multiple-view ANPA diagnostic may resolve detailed fast-ion density evolution during the EP-mode excitation process.

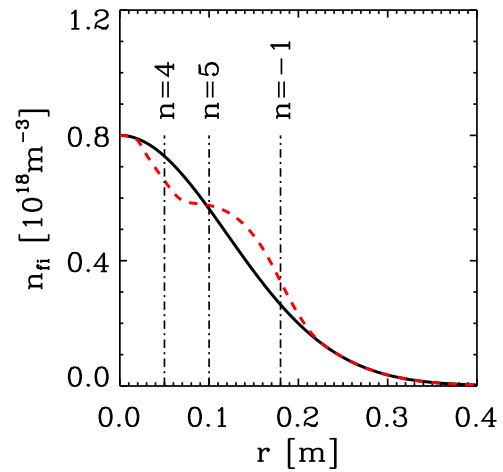


FIG. 19. Proposed fast-ion density profile ( $n_{fi}$ ) relaxation process to illustrate a potential EP-mode excitation sequence: black solid line indicates the initial profile before the onset of EP instabilities and red dashed line is the redistributed profile with local flattening near the maximum of the  $n = 5$  EP mode. The vertical dashed lines correspond to the measured electron-density-fluctuation peak-locations ( $|R - R_{mag}|$ ) of multiple EP-modes (see Figs. 7 and 8).

Detailed measurements of fast-ion distribution function may also contribute to our understanding of the strong inboard-outboard asymmetric structure of line-integrated density fluctuations.

The identity of the detected EP modes remains ambiguous. The  $n = 5$  mode is likely a continuum mode destabilized by the strong fast ion density gradient, judged by the dependence of the  $n = 5$  frequency on the beam ion species (Fig. 9). The  $n = 4$  mode may be an Alfvén eigenmode, as its frequency exhibits an Alfvénic scaling and occurs near the magnetic axis where the damping is minimal. Recent numerical calculations found an  $n = 4$  GAE with frequency and structure similar to experimental measurements.<sup>48</sup> A joint experimental and theoretical effort is required to further our understanding.

One objective of the EP community is to develop predictive capability for fast-ion driven instabilities. The newly emerging EP physics in the RFP configuration which exhibits its fascinating nonlinear evolution and strong wave-particle interactions provides a new and complementary environment to test and challenge our current understanding of EP physics and improve our confidence in predictive capability.

## ACKNOWLEDGMENTS

The authors are grateful to helpful discussions with Professor B. Breizman, Dr. G. Fu, Professor W. W. Heidbrink, Dr. G. Kramer, Dr. D. A. Spong, and Dr. L. Zheng, and much assistance from the TRANSP development team at PPPL. The experimental work was made possible with the support from the MST group. In particular, the authors thank J. Clark, J. Kim, Dr. J. Waksman for beam operation, and Dr. K. J. McCollam for discussion on F-scan experiment. This work was supported by U.S. Department of Energy.

<sup>1</sup>ITER Physics Basis, *Nucl. Fusion* **39**, 2471 (1999).

<sup>2</sup>A. Fasoli, C. Gormenzano, H. L. Berk, B. Breizman, S. Briguglio, D. S. Darrow, N. Gorelenkov, W. W. Heidbrink, A. Jaun, S. V. Konovalov,

- R. Nazikian, J.-M. Noterdaeme, S. Sharapov, K. Shinohara, D. Testa, K. Tobita, Y. Todo, G. Vlad, and F. Zonca, *Nucl. Fusion* **47**, S264 (2007).
- <sup>3</sup>K. L. Wong, *Plasma Phys. Controlled Fusion* **41**, R1 (1999).
- <sup>4</sup>W. W. Heidbrink, *Phys. Plasmas* **15**, 055501 (2008).
- <sup>5</sup>H. H. Duong, W. W. Heidbrink, E. J. Strait, T. W. Petrie, R. Lee, R. A. Moyer, and J. G. Watkins, *Nucl. Fusion* **33**, 749 (1993).
- <sup>6</sup>S. E. Sharapov, B. Alper, H. L. Berk, D. N. Borba, B. N. Breizman, C. D. Challis, I. G. J. Classen, E. M. Edlund, J. Eriksson, A. Fasoli, E. D. Fredrickson, G. Y. Fu, M. Garcia-Munoz, T. Gassner, K. Ghantous, V. Goloborodko, N. N. Gorelenkov, M. P. Gryaznevich, S. Hacquin, W. W. Heidbrink, C. Hellesen, V. G. Kiptily, G. J. Kramer, P. Lauber, M. K. Lilley, M. Lisak, F. Nabais, R. Nazikian, R. Nyqvist, M. Osakabe, C. Perez von Thun, S. D. Pinches, M. Podesta, M. Porkolab, K. Shinohara, K. Schoepf, Y. Todo, K. Toi, M. A. Van Zeeland, I. Voitsekhovich, R. B. White, V. Yavorskij, ITPA EP TG, and JET-EFDA Contributors, *Nucl. Fusion* **53**, 104022 (2013).
- <sup>7</sup>G. Y. Fu and J. W. Van Dam, *Phys. Fluids B* **1**, 1949 (1989).
- <sup>8</sup>R. Lorenzini, E. Martinez, P. Piovesan, D. Terranova, P. Zanca, M. Zuin, A. Alfieri, D. Bonfiglio, F. Bonomo, A. Canton, S. Cappello, L. Carraro, R. Cavazzana, D. F. Escande, A. Fassina, P. Franz, M. Gobbin, P. Innocente, L. Marrelli, R. Pasqualotto, M. E. Puiatti, M. Spolaore, M. Valisa, N. Vianello, P. Martin, and RFX-mod Team and Collaborators, *Nat. Phys.* **5**, 570 (2009).
- <sup>9</sup>Ya. I. Kolesnichenko, A. Könies, V. V. Lutsenko, and Yu. V. Yakovenko, *Plasma Phys. Controlled Fusion* **53**, 024007 (2011).
- <sup>10</sup>G. Regnoli, H. Bergsäter, E. Tennfors, F. Zonca, E. Martinez, G. Serianni, M. Spolaore, N. Vianello, M. Cecconello, V. Antoni, R. Cavazzana, and J.-A. Malmberg, *Phys. Plasmas* **12**, 042502 (2005).
- <sup>11</sup>S. Spagnolo, M. Zuin, F. Auremma, R. Cavazzana, E. Martinez, M. Spolaore, and N. Vianello, *Nucl. Fusion* **51**, 083038 (2011).
- <sup>12</sup>R. M. Magee, D. J. Den Hartog, S. T. A. Kumar, A. F. Almagri, B. E. Chapman, G. Fiksel, V. V. Mirnov, E. D. Mezonlin, and J. B. Titus, *Phys. Rev. Lett.* **107**, 065005 (2011).
- <sup>13</sup>J. J. Koliner, C. B. Forest, J. S. Sarff, J. K. Anderson, D. Liu, M. D. Nornberg, J. Waksman, L. Lin, D. L. Brower, W. X. Ding, and D. A. Spong, *Phys. Rev. Lett.* **109**, 115003 (2012).
- <sup>14</sup>L. Lin, W. X. Ding, D. L. Brower, J. J. Koliner, S. Eilerman, J. A. Reusch, J. K. Anderson, M. D. Nornberg, J. S. Sarff, J. Waksman, and D. Liu, *Phys. Plasmas* **20**, 030701 (2013).
- <sup>15</sup>R. N. Dexter, D. W. Kerst, T. W. Lovell, S. C. Prager, and J. C. Sprott, *Fusion Technol.* **19**, 131 (1991).
- <sup>16</sup>J. K. Anderson, A. F. Almagri, B. E. Chapman, V. I. Davydenko, P. Deichuli, D. J. Den Hartog, C. B. Forest, G. Fiksel, A. A. Ivanov, D. Liu, M. D. Nornberg, J. S. Sarff, N. Stupishin, and J. Waksman, *Trans. Fusion Sci. Technol.* **18**, 27 (2011).
- <sup>17</sup>J. K. Anderson, A. F. Almagri, D. J. Den Hartog, S. Eilerman, C. B. Forest, J. J. Koliner, V. V. Mirnov, L. A. Morton, M. D. Nornberg, E. Parke, J. A. Reusch, J. S. Sarff, J. Waksman, V. Belykh, V. I. Davydenko, A. A. Ivanov, S. V. Polosatkin, Y. A. Tsidulko, L. Lin, D. Liu, G. Fiksel, H. Sakakita, D. A. Spong, and J. Titus, *Phys. Plasmas* **20**, 056102 (2013).
- <sup>18</sup>D. L. Brower, W. X. Ding, S. D. Terry, J. K. Anderson, T. M. Biewer, B. E. Chapman, D. Craig, C. B. Forest, S. C. Prager, and J. S. Sarff, *Phys. Rev. Lett.* **88**, 185005 (2002).
- <sup>19</sup>B. H. Deng, D. L. Brower, W. X. Ding, M. D. Wyman, B. E. Chapman, and J. S. Sarff, *Rev. Sci. Instrum.* **77**, 10F108 (2006).
- <sup>20</sup>L. Lin, W. X. Ding, and D. L. Brower, *Rev. Sci. Instrum.* **83**, 10E320 (2012).
- <sup>21</sup>J. K. Anderson, C. B. Forest, T. M. Biewer, J. S. Sarff, and J. C. Wright, *Nucl. Fusion* **44**, 162 (2004).
- <sup>22</sup>E. M. Edlund, M. Porkolab, G. J. Kramer, L. Lin, Y. Lin, and S. J. Wukitch, *Phys. Rev. Lett.* **102**, 165003 (2009).
- <sup>23</sup>S. E. Sharapov, B. Alper, J. Fessey, N. C. Hawkes, N. P. Young, R. Nazikian, G. J. Kramer, D. N. Borba, S. Hacquin, E. De La Luna, S. D. Pinches, J. Rapp, D. Testa, and JET-EFDA Contributors, *Phys. Rev. Lett.* **93**, 165001 (2004).
- <sup>24</sup>M. A. Van Zeeland, G. J. Kramer, R. Nazikian, H. L. Berk, T. N. Carlstrom, and W. M. Solomon, *Plasma Phys. Controlled Fusion* **47**, L31 (2005).
- <sup>25</sup>J. A. Reusch, J. K. Anderson, V. Belykh, S. Eilerman, D. Liu, G. Fiksel, and S. Polosatkin, *Rev. Sci. Instrum.* **83**, 10D704 (2012).
- <sup>26</sup>S. Eilerman, J. K. Anderson, J. A. Reusch, D. Liu, G. Fiksel, S. Polosatkin, and V. Belykh, *Rev. Sci. Instrum.* **83**, 10D302 (2012).
- <sup>27</sup>R. Goldston, D. McCune, H. Towner, S. Davis, R. Hawryluk, and G. Schmidt, *J. Comput. Phys.* **43**, 61 (1981).
- <sup>28</sup>A. Pankin, D. McCune, R. Andre, G. Bateman, and A. Kritiz, *Comput. Phys. Commun.* **159**, 157 (2004).
- <sup>29</sup>J. S. Sarff, A. F. Almagri, J. K. Anderson, M. Borchardt, D. Carmody, K. Caspary, B. E. Chapman, D. J. Den Hartog, J. Duff, S. Eilerman, A. Falkowski, C. B. Forest, J. A. Goetz, D. J. Holly, J.-H. Kim, J. King, J. Ko, J. Koliner, S. Kumar, J. D. Lee, D. Liu, R. Magee, K. J. McCollam, M. McGarry, V. V. Mirnov, M. D. Nornberg, P. D. Nonn, S. P. Oliva, E. Parke, J. A. Reusch, J. P. Sauppe, A. Seltzman, C. R. Sovinec, H. Stephens, D. Stone, D. Theucks, M. Thomas, J. Triana, P. W. Terry, J. Waksman, W. F. Bergerson, D. L. Brower, W. X. Ding, L. Lin, D. R. Demers, P. Fimognari, J. Titus, F. Auremma, S. Cappello, P. Franz, P. Innocente, R. Lorenzini, E. Martinez, B. Momo, P. Piovesan, M. Puiatti, M. Spolaore, D. Terranova, P. Zanca, V. Belykh, V. I. Davydenko, P. Deichuli, A. A. Ivanov, S. Polosatkin, N. V. Stupishin, D. Spong, D. Craig, R. W. Harvey, M. Cianciosa, and J. D. Hanson, *Nucl. Fusion* **53**, 104017 (2013).
- <sup>30</sup>G. Fiksel, B. Hudson, D. J. Den Hartog, R. M. Magee, R. O'Connell, S. C. Prager, A. D. Beklemishev, V. I. Davydenko, A. A. Ivanov, and Yu. A. Tsidulko, *Phys. Rev. Lett.* **95**, 125001 (2005).
- <sup>31</sup>M. Gobbin, R. B. White, L. Marrelli, and P. Martin, *Nucl. Fusion* **48**, 075002 (2008).
- <sup>32</sup>F. Porcelli, R. Stankiewicz, W. Kerner, and H. L. Berk, *Phys. Plasmas* **1**, 470 (1994).
- <sup>33</sup>S. C. Prager, A. F. Almagri, M. Cecik, J. Chapman, D. J. Den Hartog, G. Fiksel, C. Hegna, H. Ji, J. S. Sarff, J. R. Drake, S. Mazur, P. Nordlund, and H. E. Saetherblom, *Plasma Phys. Controlled Fusion* **37**, A303 (1995).
- <sup>34</sup>L. Chen and F. Zonca, *Nucl. Fusion* **47**, S727 (2007).
- <sup>35</sup>H. Ji, S. C. Prager, A. F. Almagri, J. S. Sarff, Y. Yagi, Y. Hirano, K. Hattori, and H. Toyama, *Phys. Plasmas* **3**, 1935 (1996).
- <sup>36</sup>L. Lin, W. X. Ding, D. L. Brower, W. F. Bergerson, and T. F. Yates, *Rev. Sci. Instrum.* **81**, 10D509 (2010).
- <sup>37</sup>Y. Todo, *Phys. Plasmas* **13**, 082503 (2006).
- <sup>38</sup>W. S. Harris, D. J. Den Hartog, and N. C. Hurst, *Rev. Sci. Instrum.* **81**, 10D505 (2010).
- <sup>39</sup>D. R. Demers and P. J. Fimognari, *Rev. Sci. Instrum.* **83**, 10D711 (2012).
- <sup>40</sup>H. L. Berk, J. W. Van Dam, Z. Guo, and D. M. Lindberg, *Phys. Fluids B* **4**, 1806 (1992).
- <sup>41</sup>C. Z. Cheng, N. N. Gorelenkov, and C. T. Hsu, *Nucl. Fusion* **35**, 1639 (1995).
- <sup>42</sup>G. J. Kramer, C. Z. Cheng, Y. Kusama, R. Nazikian, S. Takeji, and K. Tobita, *Nucl. Fusion* **41**, 1135 (2001).
- <sup>43</sup>E. J. Strait, W. W. Heidbrink, A. D. Turnbull, M. S. Chu, and H. H. Duong, *Nucl. Fusion* **33**, 1849 (1993).
- <sup>44</sup>W. W. Heidbrink, H. H. Duong, J. Manson, E. Wilfrid, C. Oberman, and E. J. Strait, *Phys. Fluids B* **5**, 2176 (1993).
- <sup>45</sup>H. L. Berk, B. N. Breizman, J. Fitzpatrick, M. S. Pekker, H. V. Wong, and K. L. Wong, *Phys. Plasmas* **3**, 1827 (1996).
- <sup>46</sup>H. L. Berk, B. N. Breizman, J. Candy, M. Pekker, and N. V. Petviashvili, *Phys. Plasmas* **6**, 3102 (1999).
- <sup>47</sup>M. Schneller, Ph. Lauber, M. Brüdgam, S. D. Pinches, and S. Günter, *Nucl. Fusion* **52**, 103019 (2012).
- <sup>48</sup>H. Cai, G. Fu, L. Lin, D. Y. Liu, W. X. Ding, D. L. Brower, and Y. J. Hu, *Phys. Plasmas* **21**, 022513 (2014).